Dynamics of pinch-off in liquid/liquid jets with surface tension

E.K. Longmire [*], T.L. Norman, D.L. Gefroh

Department of Aerospace Engineering and Mechanics, University of Minnesota, Minneapolis, MN 55455, USA

Abstract

Full two-dimensional velocity fields were measured by PIV in forced jets of glycerin/water solution flowing into and pinching off in ambients of Dow Corning 200 Series silicone fluid. The Reynolds, Froude, and Bond numbers computed at the nozzle exit were 34, 0.20, and 6.1, respectively. Viscosity ratios between the inner and outer fluids of 0.17 and 1.7 were examined in jets forced at a Strouhal number of 4.0. The experiments revealed that the viscosity ratio strongly affected the evolving jet flow, the pinch-off process, and the resulting droplet shapes. The higher viscosity ambient yielded less gravitational acceleration within the jet fluid, a broader cone shape upstream and a more rounded drop interface downstream of the pinch-off zone, and eventually spheroidal droplets with weak oscillations in shape. The lower viscosity ambient yielded greater gravitational acceleration within the jet, a narrower cone shape upstream and flatter drop interface downstream of the pinch-off zone, and eventually strong oscillations including inverted curvature within the droplets that formed. The difference in downstream interface angles at pinch off could be explained by the velocity and vorticity distributions within the two flows. © 2001 Elsevier Science Ltd. All rights reserved.

Keywords: Jet; PIV; Immiscible liquids; Surface tension; Topological transition; Viscosity

1. Introduction

In this paper, we describe results from experiments conducted in liquid/liquid mixtures with significant interfacial tension. The break up of a continuous jet into discrete droplets is examined in detail as an example of a topological transition. In general, topological transitions, which are associated with very small length and time scales, are difficult to observe or characterize, especially in flows with significant inertia. The small length and time scales accompanying transitions also cause singularities in continuum-based numerical simulations. Numerical simulations thus require

[*] Corresponding author.

E-mail address: longm001@umn.edu (E.K. Longmire).

some type of model in order to bridge or evolve through a transition. In the current study, experiments and methods were developed to obtain instantaneous velocity and vorticity fields on both sides of a liquid/liquid interface. The methods were then applied to track these fields through transitions. The results thus provide realistic yet geometrically simple flow cases that can be used to test numerical transition models.

Round liquid jets flowing into a second immiscible liquid have been investigated by many researchers due to their fundamental simplicity as well as their importance in a number of industrial systems. Extensive measurements of jet break up length and downstream droplet size have been made by Meister and Scheele (1969a,b), Skelland and Johnson (1974), and Bright (1985), for example. These researchers determined average jet break-up length in terms of injection Reynolds number for a variety of fluid combinations. Skelland and Walker (1989) performed similar experiments in fluids containing surfactants. The experiments demonstrated that for low flow rates (and Reynolds number), droplets form at and detach from the jet outlet. As the flow rate is increased, the injected fluid forms a jet which develops axisymmetric instabilities and pinches off at a finite length. Above a Reynolds number associated with the maximum length, three-dimensional instabilities and eventually direct atomization occur. The Reynolds number range corresponding to each flow mode depends significantly on the other system parameters, including the fluid properties. In addition, Freeman and Tavlarides (1979) and Kitamura et al. (1982) showed that co-flowing surrounding streams could be applied to suppress jet instabilities. In general, the above studies did not examine the details of the transition region or determine local velocities within the flow.

With most fluid combinations, refractive effects make it difficult to view beyond the external surface of the jet column, and therefore few quantitative local or instantaneous measurements have been reported. Tadrist et al. (1991) took advantage of refractive effects and employed a laser scattering method to measure instantaneous jet diameter and fluctuation frequency at specific axial locations. Richards and Scheele (1985) used flash photolysis and optical corrections to track tracers and deduce axial velocity profiles inside of xylene jets flowing into water. The transition region near pinch off was not examined. Recent experiments by Zhang and Basaran (1995) focused on transition behavior in dripping flows surrounded by air. The authors examined the effect of various input parameters on the details of the developing drop shape, neck formation, and eventual pinch off. A high-speed digital camera was employed to document the time evolution of drop length, volume, and shape. Brenner et al. (1997) and Cohen et al. (1999) used similar methods to analyze interface position and shape surrounding pinch off for dripping liquids in air and dripping liquids in a liquid, respectively. Finally, McKinley and Tripathi (2000) measured the variation of neck diameter vs. time for a pinching thread in air to very high accuracy.

The objective of the current study is to examine the detailed dynamics of the pinch-off process in a round jet flow where a number of fluid parameters, including inertia and the viscosity of the outer fluid, are important. As described below, sinusoidal velocity perturbations are imposed on the mean flow to ensure periodic and repeatable pinch-off at the perturbation frequency. This enables us to examine any phase in the transition cycle. In addition, we apply an index of refraction matching technique in order to visualize the flow both interior and exterior to the jet. This allows us to obtain velocity measurements of the entire flow field at a given instant. Finally, the velocity measurements are differentiated to reveal evolving vorticity fields across the fluid interface.

2. Experimental facility and method

The experiments were performed in a closed-loop facility with test section dimensions of 56 cm × 20.3 cm × 20.3 cm (see Fig. 1). The flow is driven by a magnetic-drive pump, and the mean velocity is controlled by a needle valve. Upstream of the test section, the flow passes through a honeycomb straightener before it is accelerated through a round nozzle with 16.5:1 area ratio and 1 cm exit diameter. The flow circuit contains a piston-driven forcer that can be used to superpose a sinusoidal perturbation on the nozzle exit velocity. The forcer was employed to generate repeatable, phase-locked pinch-off conditions. The mean flow rate was determined with a flow meter calibrated for the circulating jet fluid.

Two series of experiments were performed. In the first series, the test section was filled to a height of 37 cm with a solution of glycerin in water. The remainder of the tank (about 19 cm of depth) was filled with Dow Corning 200 fluid (I). In the second series, a less viscous Dow Corning 200 fluid (II) constituted the upper layer, and the lower and upper layers measured 28 and 25 cm in depth, respectively. In all of the experiments, the glycerin/water solution was pumped around the flow loop and injected through the nozzle, which was submerged in the Dow Corning fluid. The two fluid combinations were chosen in order that the indices of refraction could be reasonably well matched, a necessary condition for clear flow visualization and PIV images. The material properties of the three fluids used are listed in Table 1.
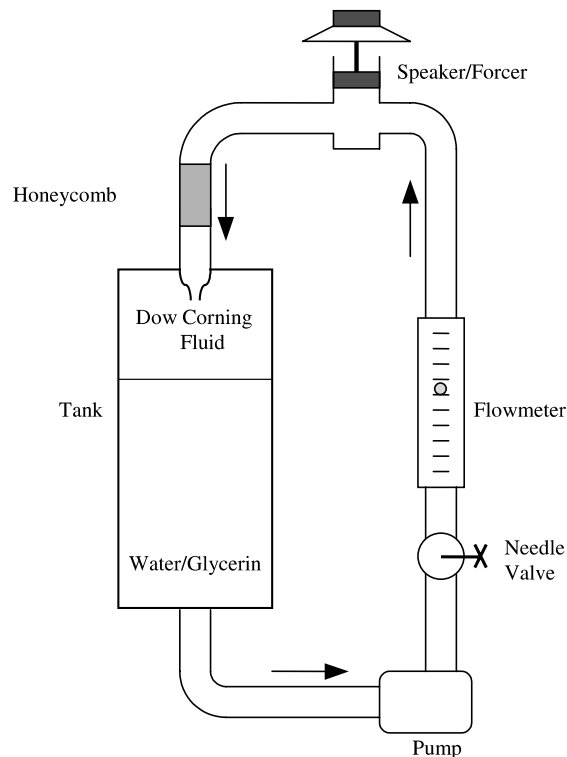

Fig. 1. Recirculating jet facility.

Table 1
Fluid properties

Fluid	Density (ρ) (g/cm^3)	Viscosity (μ) (cP)	Refractive index
Dow Corning 200 (I)(50 cs)	0.96	48.0	1.401
Dow Corning 200 (II)(5 cs)	0.97	4.85	1.394
Water/Glycerin (56% wt. Glycerin)	1.14	8.33	1.407

For PIV measurements, titanium dioxide seed particles ($d \sim 3$ μm) were added to both the jet and ambient fluids. In the experiments with Dow Corning Fluid I, the jet fluid was seeded more heavily in order that the interface location could be distinguished. In the experiments with Dow Corning Fluid II, both fluids were seeded at similar number densities, and a small quantity of Rhodamine 6G dye was added to the jet fluid to mark the interface location more precisely. Prior to PIV analysis, images were filtered with a preprocessing routine to remove the 'dyed' background. The interfacial tension between the water/glycerin solution and Dow Corning Fluid I was measured with a spinning drop tensiometer to be 29.5 mN/m for both seeded and unseeded fluids. It is assumed that the water/glycerin solution and Dow Corning Fluid II exhibit a similar value.

Two frequency-doubled Nd:YAG lasers (Continuum Surelite I) pulsed in rapid succession were used to illuminate flow images. Both beams were directed through a spherical (1 m focal length) and a cylindrical (19 cm focal length) lens aligned to generate vertical sheets that intersected the jet axis. Sets of 'double exposure' images were captured with a Kodak DCS 420M digital camera and a Nikon AF Micro-Nikkor 105 mm lens. For measurements with increased magnification, an extender ring was mounted between the camera and the lens. The camera array contained 1012×1524 pixels with 8-bit pixel depth. The camera viewed the flow field through a mirror that oscillated about its vertical axis in order to produce a known horizontal shift in each double exposure image. The time between laser pulses and the mirror rotation speed were optimized to achieve displacements between particle pairs of approximately 8 pixels in a given image. Images at high magnification required a larger pixel displacement to avoid overlapping particle pairs.

Timing and control signals were generated by a National Instruments NB-MIO-16X board installed in a Macintosh computer. These signals were employed to drive the forcer as well as an external timing circuit that controlled the mirror rotation, laser pulsing, and camera shutter release. The forcer was driven by an audio speaker attached to the piston. A diagram of the instrumentation set up is shown in Fig. 2.

Acquired images were transferred either directly or via PCMCIA cards to a Pentium-based PC for analysis. Individual images were analyzed with a single frame cross-correlation routine in Visiflow software. For cases with a viscosity ratio (inner to outer fluid) of $\lambda = 0.17$, two-dimensional vector fields were computed using interrogation areas with 64 pixels on a side (equivalent to 1.35 mm) and 50% overlap (see Figs. 4, 5, 7 and 12) or areas with 128 pixels on a side (equivalent to 1.04 mm) and 75% overlap (see Figs. 9 and 11). For cases with a viscosity ratio of $\lambda = 1.7$, all interrogation areas were 64 pixels on a side with 50% overlap. Each interrogation area corresponded to a dimension of 2.69 mm for low resolution measurements (Figs. 3, 6 and 8) and 0.84 mm for high resolution measurements (Figs. 10 and 12). Vorticity fields were determined by calculating line integrals using the eight vectors surrounding each position, and dividing by the
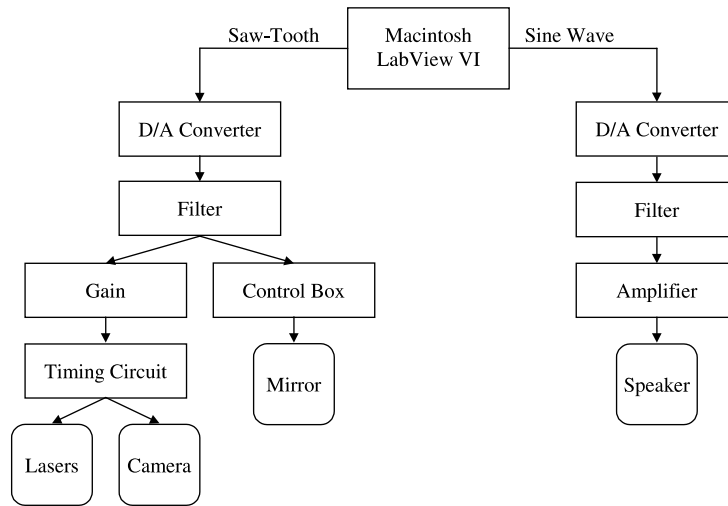
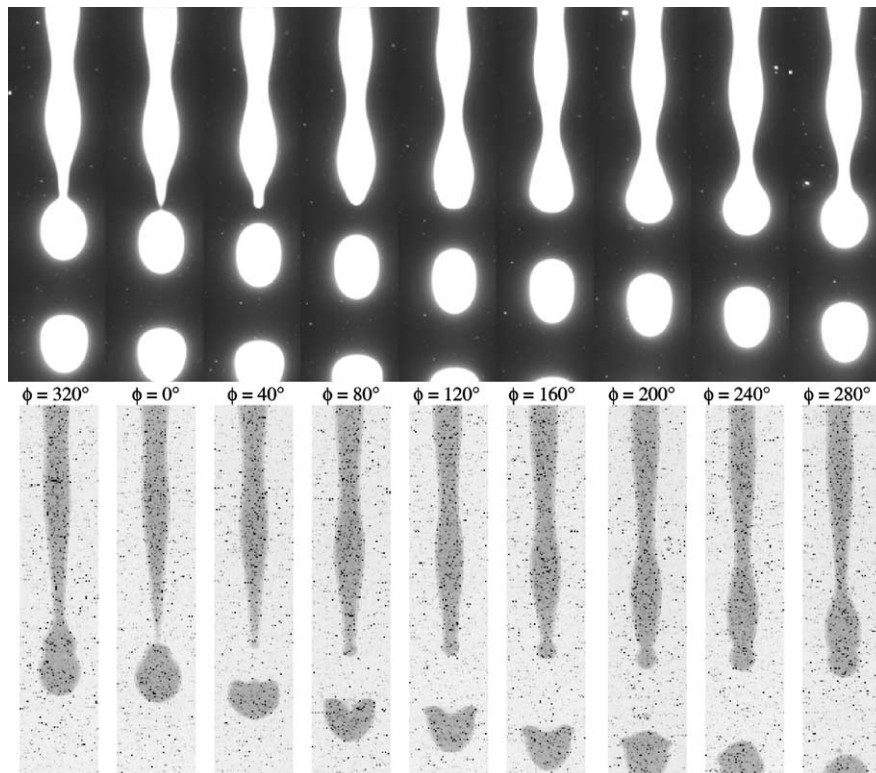Fig. 2. PIV instrumentation and control diagram.

Fig. 3. Images of phase-locked flow. Upper sequence is $\lambda = 0.17$, $Re = 50$. Length of each image is $6.5D$. Lower sequence is $\lambda = 1.7$, $Re = 35$. Length of each image is $6.4D$.

area within the closed contour. All vorticity contours were normalized by the ratio of jet exit velocity to jet exit diameter (U_e/D).

3. Results

The cases examined represented a parameter set where the fluid properties as well as inertia, gravity, and surface tension are all significant. The flow conditions can be characterized by a set of five dimensionless parameters:

$$\frac{\rho_i}{\rho_o}, \quad \frac{\mu_i}{\mu_o}, \quad Re = \frac{\rho_i U_e D}{\mu_i}, \quad Fr = \frac{U_e \sqrt{\rho_i}}{\sqrt{\Delta\rho g D}}, \quad Bo = \frac{\Delta\rho g D^2}{\sigma},$$

where the subscripts i and o denote the jet and ambient fluids, ρ is the density, μ is the viscosity, $\Delta\rho$ is the density difference between fluids, g is the gravitational constant, and σ is the interfacial tension. The values of these parameters for the two flow cases are listed in Table 2. In general, the Reynolds, Froude, and Bond numbers and the density ratio were held constant for the two experimental series, while the viscosity ratio was varied by an order of magnitude. The conditions using Dow Corning I match those for PIV measurements reported in Longmire et al. (1999) and correspond closely with laser induced fluorescence visualization reported in Webster and Longmire (2001).

Under the chosen flow conditions, gravitational effects cause the jet to accelerate and contract immediately after exiting the nozzle. In the absence of forcing, the above conditions yield a smooth jet column that travels all the way to the downstream fluid interface without developing any significant waves or instabilities. When the flow is forced with a sinusoidal velocity perturbation, however, instabilities are enhanced, and pinch off occurs within the layer of Dow Corning fluid. The pinch-off location can be controlled by adjusting the forcing amplitude such that increasing the amplitude moves the pinch-off location upstream.

For the cases described below, the flow was forced at the laser pulsing frequency of 10 Hz yielding a Strouhal number $St = fD/U_e$ of about 4. The forcing amplitude was chosen as the minimum required to achieve a jetting (as opposed to dripping) flow with a phase-locked pinch-off condition. The case with a viscosity ratio of $\lambda = 0.17$ required a large forcing amplitude (the peak-to-peak voltage input to the speaker was 20 V), probably because of the stabilizing influence of the high viscosity ambient. Under the chosen conditions, one drop formed during each forcing cycle at a location approximately seven diameters downstream of the nozzle exit. The $\lambda = 1.7$ case

Table 2
Dimensionless flow parameters using nozzle exit diameter and velocity

Parameter	I	II
Re	34	35.2
Fr	0.20	0.21
Bo	6.1	6.1
ρ_i/ρ_o	1.19	1.18
$\lambda = \mu_i/\mu_o$	0.17	1.72
St	4.0	3.9

required a much lower forcing amplitude of 5.2 V to achieve a jet of similar length. (Increasing the amplitude caused the pinch-off location to move upstream.) Under these conditions, a stable 'single drop mode' was more difficult to achieve. In particular, each larger drop was sometimes accompanied by the formation of a small satellite drop. This result suggests that the preferred pinch-off frequency is higher for $\lambda = 1.7$ than for $\lambda = 0.17$, a trend consistent with calculations by Meister and Scheele (1967) who performed a stability analysis on cylindrical jets surrounded by fluids with significant viscosity. The results presented below for $\lambda = 1.7$ were obtained typically when no satellite drop was present.

Two sequences of phase-locked images of forced flow are given in Fig. 3. The upper sequence shows $\lambda = 0.17$ at a slightly higher Reynolds number than the value given in Table 2 ($Re = 50$ instead of $Re = 35$). The lower sequence was obtained for the flow conditions listed in Table 2 for $\lambda = 1.7$. The jet fluid is marked by Rhodamine 6G, and the image brightness is inverted. This sequence was chosen in order to match the field of view as closely as possible with the lower sequence. The flow moves from top to bottom in all cases, and the phase corresponding to pinch off ($\phi = 0°$) is the second in each series. In both sequences, axisymmetric waves develop upstream of the pinch-off location. When $\lambda = 0.17$, round drops form on the end of the jet, and the local curvature at the jet/drop connection decreases steadily until the interface slope appears discontinuous. The pinch-off region is characterized by a conical section that necks down to very small diameter while remaining connected to the round drop forming downstream. After pinch off, the thin neck recoils to decrease the local curvature. A new drop begins to form as the 'wide' part of a wave travels to the end of the jet. The angle between the fluid interface upstream of the pinch off and the horizontal plane measures 68–74° (given experimental uncertainty), and the angle between the horizontal and the downstream fluid interface is 23°. Closer to the pinch-off point, however, this angle is significantly smaller ($\sim$11°) (refer to Webster and Longmire, 2001). After pinch off, the drops have the shape of prolate spheroids. The upstream end of each drop flattens initially as it begins to propagate downstream. Photographs showing a larger field of view (see Webster and Longmire, 2001) reveal weak oscillations in shape as the drops continue to travel through the Dow Corning fluid. No 'overturning' or inversion of the drop surface occurs.

When $\lambda = 1.7$, the variations in diameter upstream of the pinch off have a longer wavelength ($\sim$2.5D vs. 2.1D) suggesting a larger wave propagation speed. This result is interesting considering that the jet exit velocity was lower for this case than for $\lambda = 0.17$. It is most likely explained by the difference in viscosities of the outer fluids. The lower viscosity ambient ($\lambda = 1.7$) offers less resistance to the inner jet fluid, and hence the jet accelerates to a higher velocity than in the corresponding case. This explanation is consistent with the measured jet velocities discussed below.

The shape of the evolving jet tip is more complex in the case with the lower viscosity ambient. Specifically, the jet tip develops a small spherical structure before the wide part of a wave approaches (see $\phi = 160°$). The spherical structure grows in diameter as the wide cross section nears and eventually intersects it. Before pinch off (see $\phi = 320°$), the spherical structure has a larger diameter than the section immediately behind it, but a local (or harmonic) concavity in curvature persists. The jet breaks off upstream of both of these sections such that the local concavity lies within the newly-formed drop. At pinch off, the upstream end of the drop has flattened, while the attached conical section is long and thin. The angle between the interface upstream of the pinch off and the horizontal plane measures 78–84°, while the angle between horizontal and the drop interface downstream is only 4–7°.

The larger upstream angle observed at pinch off for this case appears to occur because of a combination of factors. First, the jet column is narrower on average in this case as pinch off is approached. Second, the jet column wavelength is longer for this case, and the local maximum in jet diameter is far upstream of the pinch-off location ($\sim$0.8 wavelengths) when $\phi = 0°$. In contrast, the $\lambda = 0.17$ case has a shorter wavelength, and the maximum in diameter lies relatively closer to the pinch-off location ($\sim$0.6 wavelengths) when $\phi = 0°$. These differences most likely occur because of the smaller viscous force impeding the flow when $\lambda = 1.7$. The difference in the downstream angles at pinch off is discussed below in the context of the local vorticity fields.

The tangents of the angles measured for both values of λ can be compared directly with pinch-off slopes found by Zhang and Lister (1999) using a boundary integral method and by Cohen et al. (1999) in a dripping flow. Our measured 'jet' pinch-off angles agree within uncertainty with the plots of s_+ ('steep cone slope') published in Zhang and Lister. Also, our measured 'drop' pinch-off angles follow the same trend of decreasing angle with increasing λ, but $\lambda = 0.17$ yields a slightly larger angle than the corresponding 'shallow cone slope' in Zhang and Lister. (The boundary integral results yield 6° for $\lambda = 0.17$.) As stated earlier, the drop pinch-off angles decrease significantly as pinch off is approached, and it is therefore possible that our measured angle would decrease somewhat if we could track the neck region to smaller scales. Also, since our visualization sequences were obtained using phase locking, they do not represent real time sequences of a single pinch off. Therefore, we cannot determine the rate of neck thinning (see e.g. McKinley and Tripathi, 2000) from the present data with any degree of certainty.

The lower viscosity ambient allows strong oscillations in the drops that break off from the jet. Immediately after pinch off, the upstream end of the drop propagates much more quickly than the downstream end, resulting in axial compression of the drop and then inverted or concave curvature on the upstream end. Interfacial tension causes the upstream surface to recover to a convex shape as the drop passes out of the field of view. The shape oscillation also generates a cusp-like structure at the location of greatest drop diameter (see $\phi = 120$–200°). The 'cusp' initiates near the upstream end of the drop, and eventually propagates toward the downstream end (see $\phi = 240°$). Additional observations and videotapes show that strong oscillations persist until the drops intersect the fluid interface downstream.

Images of four phases of seeded flow with $\lambda = 0.17$ and $Re = 34$ are shown in Fig. 4. These images were employed to obtain low resolution velocity fields via PIV. A sample vector field from this flow ($\phi = 60°$) is shown in Fig. 5. For clarity, only half of all the calculated vectors are displayed. The plot gives an idea of the locations of high velocity in the flow and of the breadth of radial velocity profiles. For example, one can observe that the largest vectors correspond with the jet fluid. Between the jet tip and the droplet downstream, the velocity is decreased. Also, the downward moving jet tip drives ambient fluid away from the centerline, while the upstream side of the droplet entrains ambient fluid toward the centerline. In the region upstream of the jet tip, the average jet radius is on the order of $0.17D$, and axial velocities become very small by $r/D = 0.3$.

A vector field corresponding to the $\phi = 40°$, $\lambda = 1.7$ image in Fig. 3 is shown in Fig. 6. In this case, the vectors are plotted with 50% overlap. Note also that the image magnification was smaller in this case than in the previous plot, so that the measurements extend over a larger area. As in the previous case, the largest velocities lie within the jet and the droplet that has broken off downstream. In this flow, the average jet radius upstream is about $0.15D$, and axial velocities again drop off sharply beyond $r/D = 0.3$.
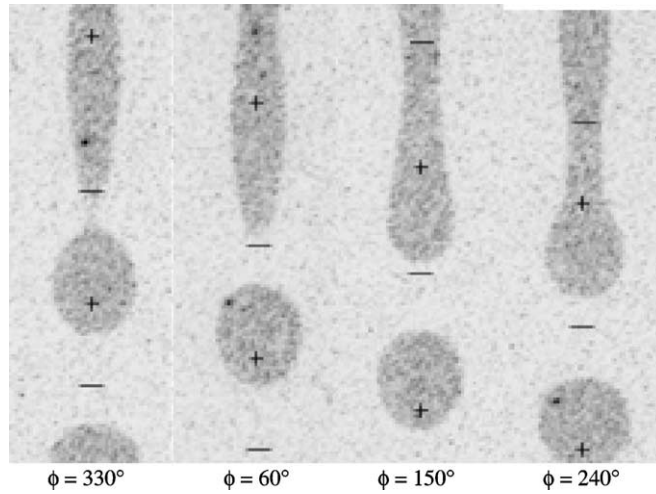
$\phi = 330°$ $\phi = 60°$ $\phi = 150°$ $\phi = 240°$

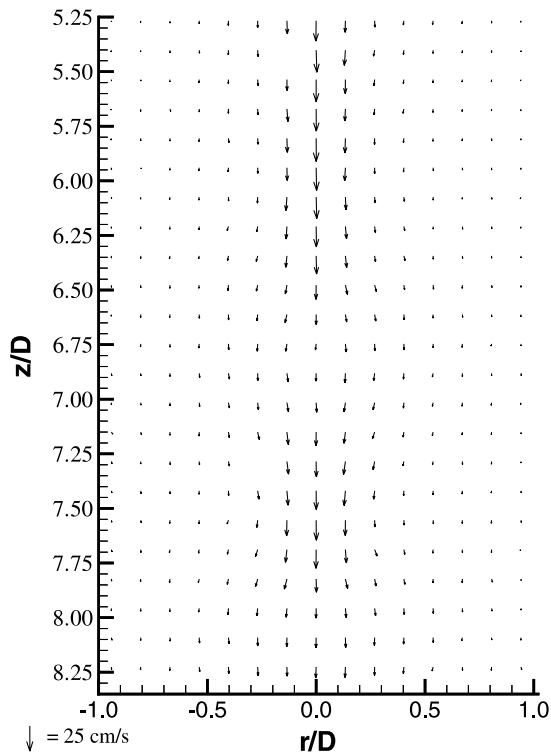Fig. 4. Images of flow for $\lambda = 0.17$, $Re = 34$. Length of each image is 3D.

Fig. 5. Low resolution vector map for $\lambda = 0.17$, $Re = 34$, $\phi = 60°$. Only 50% of all vectors are plotted.

Fig. 7 plots velocity along the jet axis as a function of downstream distance for the four phases depicted in Fig. 4. All of the values were extracted from PIV vector fields with 50% overlap. Each value plotted is the ensemble average from five plots of like forcing phase. The local maxima and
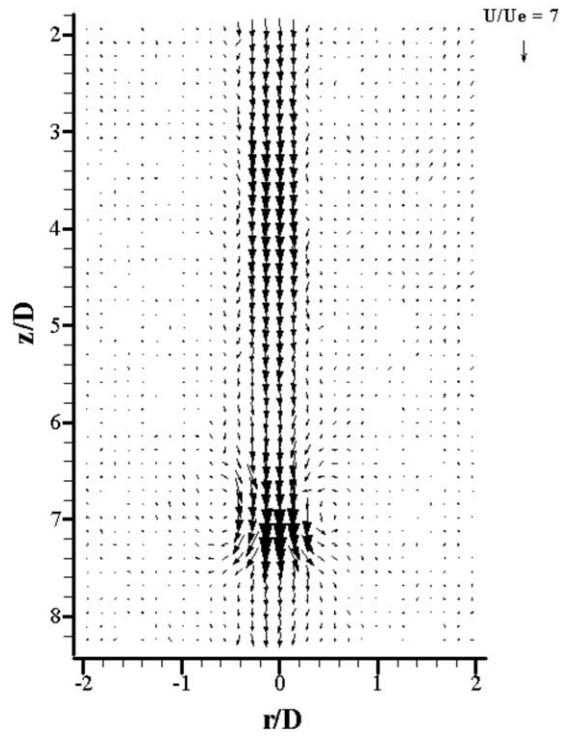
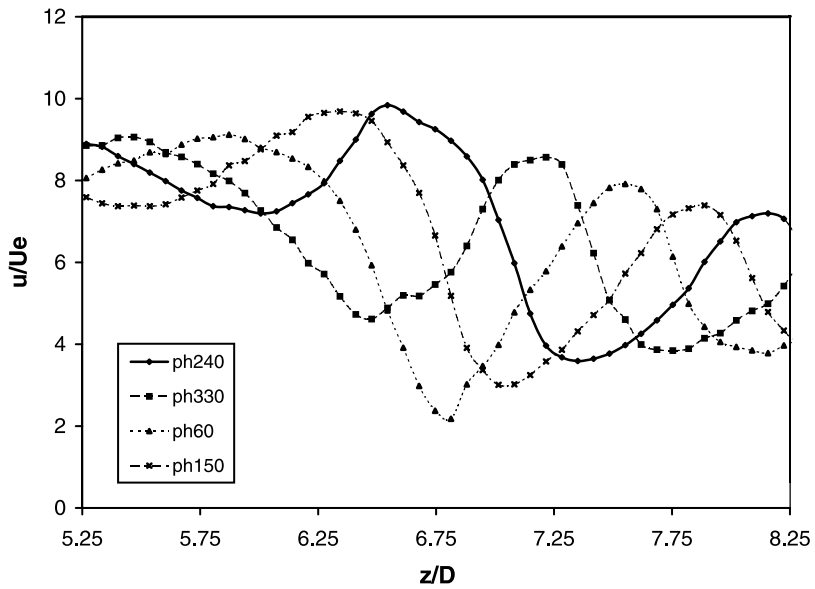Fig. 6. Low resolution vector map for $\lambda = 1.7$, $Re = 35$, $\phi = 40°$.

Fig. 7. Jet centerline velocity for $\lambda = 0.17$, $Re = 34$.

minima in velocity are marked by '+' and '−', respectively in the images in Fig. 4. At the upstream end of the plot, the normalized velocity (u/U_e) varies from 7.1 to 8.9. Examination of phase-specific velocity plots and corresponding interface locations in this zone shows that local maxima and minima in streamwise velocity occur upstream and downstream of the 'widest' part of the axisymmetric waves, respectively. Thus, the velocity maxima occur where the interface is diverging or expanding with increasing axial distance, and the minima occur where the interface is converging. This behavior, which results from the original velocity perturbation at the nozzle outlet, is consistent with the idea that the periodic forcing encourages pinch off: the forcing causes the inner fluid to be focused into distinct axial regions that eventually result in drops.

Fig. 7 shows how the variations in centerline velocity grow substantially as the pinch-off region is approached and surface tension becomes important in the flow dynamics. (Pinch off occurs at $z/D = 6.9$.) The maximum velocity plotted ($9.9U_e$ for $\phi = 240°$) occurs near a local minimum in diameter in the jet neck and is associated with inner fluid moving into the drop forming downstream. As the flow progresses, this local maximum shifts into the drop that is forming, and after the drop breaks off, the maximum persists near the drop's downstream end. The minimum velocity plotted ($2.2U_e$ for $\phi = 60°$) corresponds with the recoiling jet tip. Note how this minimum shifts downstream of and away from the jet tip as the flow progresses. After pinch off ($z/D > 7.5$), the amplitude of the velocity variation along the flow axis associated with the drops is substantial ($3.8U_e$–$7.1U_e$), and the mean velocity in this range is smaller than before pinch off.

Plots of centerline velocity for $\lambda = 1.7$ are shown in Fig. 8. The velocity values represent PIV measurements calculated from six of the seeded images in Fig. 3. Since the magnification for this image series was lower than for the images in Fig. 4, the plots extend over a greater axial distance. Also, in this series, the pinch off occurs at $z/D = 6$, slightly upstream of the location for the $\lambda = 0.17$ case in Figs. 4 and 7.
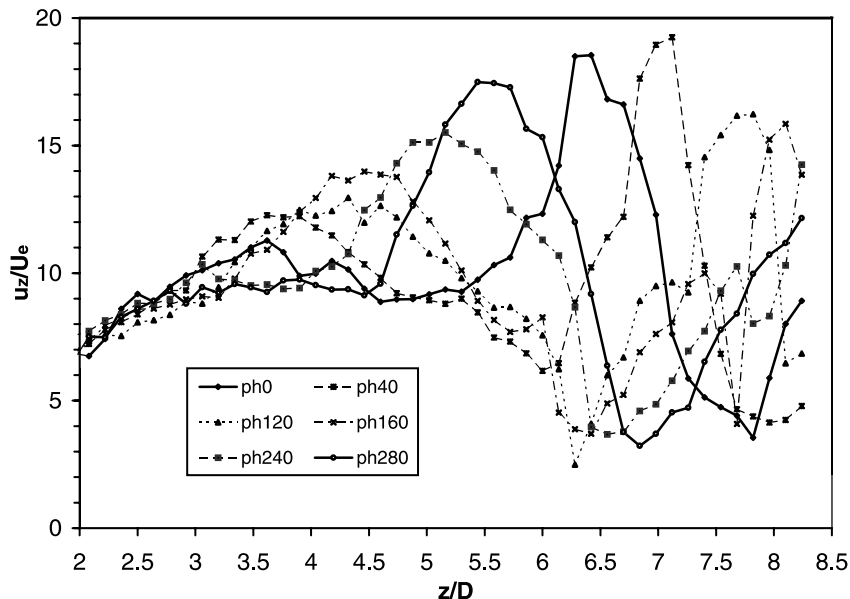

Fig. 8. Jet centerline velocity for $\lambda = 1.7$, $Re = 35$.

The first point to note about this figure is that the centerline flow accelerates fairly steadily until $z/D = 3.5$. The average velocity at this location ($u/U_e \approx 10$) already exceeds that observed for $\lambda = 0.17$ at $z/D = 5.25$. Again, we postulate that this stronger acceleration occurs because the lower viscosity ambient in this case offers less resistance to the downward flow. The lower viscosity ambient also offers less resistance to local perturbations caused by the pinch off, as is evidenced by the stronger and more complex velocity variations observed. For example, when $\phi = 0°$, a weak minimum occurs at $z/D = 4.6$, and the velocity magnitude remains relatively uniform until $z/D = 5.3$. Then, the flow accelerates sharply up to a maximum velocity of $18.5U_e$ at $z/D = 6.4$. This strong maximum lies near the center of the drop downstream of the pinch-off zone (see Fig. 3). Downstream of the drop, the velocity decreases to a minimum of similar order to that observed when $\lambda = 0.17$.

After the pinch off (see $\phi = 120°$ in Figs. 3 and 8), a strong minimum exists close to the re-coiling jet tip. The flow then accelerates with downstream distance until a weak localized minimum occurs near the upstream end of the drop. This cusp in the velocity profile coincides with the concave drop interface that has begun to rebound from its maximum deformation. The same local minimum is observed in subsequent phases up to $\phi = 240°$ and is strongest near $\phi = 160°$. The local velocity maximum inside of the drop moves toward the drop's downstream end as ϕ increases from $0°$ to $160°$. Another interesting feature appears in the plot of $\phi = 160°$. At $z/D = 6$, a local maximum exists that coincides with the upstream end of the small sphere forming on the jet tip. As in the corresponding $\lambda = 0.17$ flow, this maximum is associated with jet fluid increasing the sphere's volume.

The evolution of vorticity in the pinch-off region for $\lambda = 0.17$ is shown in Fig. 9. The vorticity plots were derived from ensemble averages of phase-locked PIV velocity fields. Corresponding seeded images are included above each vorticity plot. In general, the vorticity contours are focused within the jet fluid as might be expected because of its relatively low viscosity compared with that of the ambient.

In the first image shown ($\phi = 300°$), a region of strong vorticity occurs at the jet neck. This region surrounds the location of maximum axial velocity (for all phases measured) within the field and is associated with a volume of jet fluid moving at relatively high speed into the drop forming downstream. The zone of intense vorticity propagates forward, weakens, and decreases in size as the jet end necks down and the drop detaches. Thus, during the later stage of the pinching process, the volume of fluid entering the drop is small. After pinch off, the recoil of the jet end induces a ring of 'inverted' vorticity, which intersects the fluid interface, to develop. Although one might expect that the reverse vorticity should develop immediately after pinch off (at the latest), it was not observed in the experiments until almost $\phi = 30°$. This 'delay' is attributed to limitations in the minimum scale resolvable by the PIV measurements and the derived vorticity values. Plots of $\phi = 30°$ and subsequent phases show that the inverted ring grows in size until $\phi = 90°$. The inverted ring persists downstream of the jet end before being stretched outward, swept upstream ($\phi = 120°$), and dissipated by the approaching flow. Additional plots document the presence of the ring until at least $\phi = 150°$.

High magnification images and vorticity plots of the $\lambda = 1.7$ case are shown in Fig. 10. Here, the inner fluid was seeded with Rhodamine dye in order to mark the interface location. The magnification is smaller than in the previous figure, but the resolution of the PIV vectors is similar. The vorticity contours, which carry the same normalized values as those in Fig. 9, are
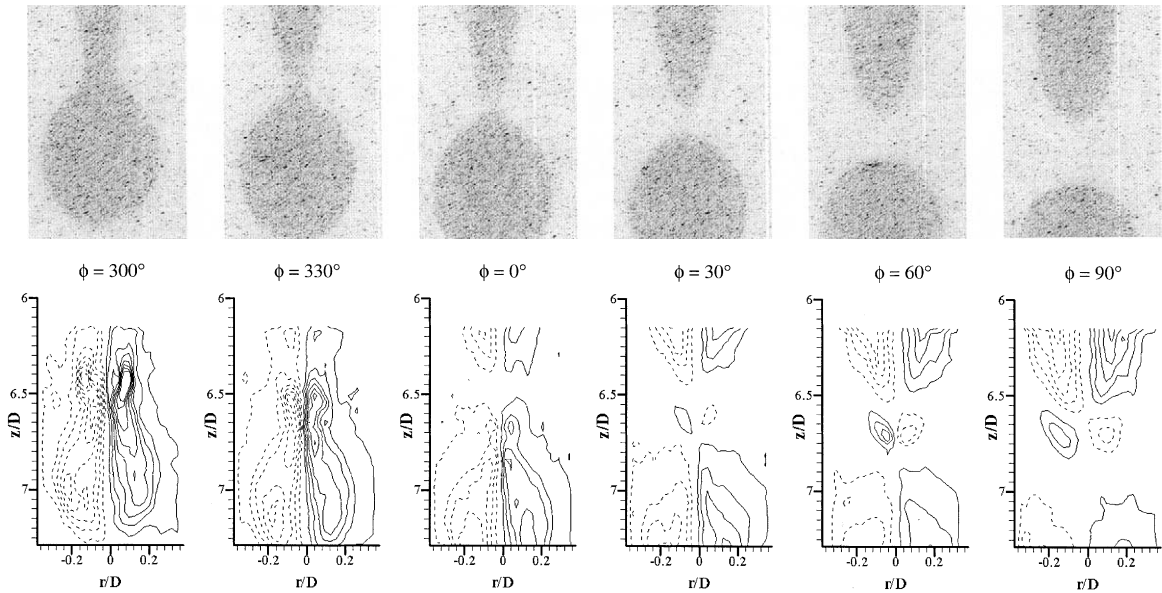
Fig. 9. Images and vorticity fields for $\lambda = 0.17$, $Re = 34$. Length of each image is 1.24D. Normalized contour levels have magnitude of 8, 16, 24, 32, 40, 48, 56, 64.
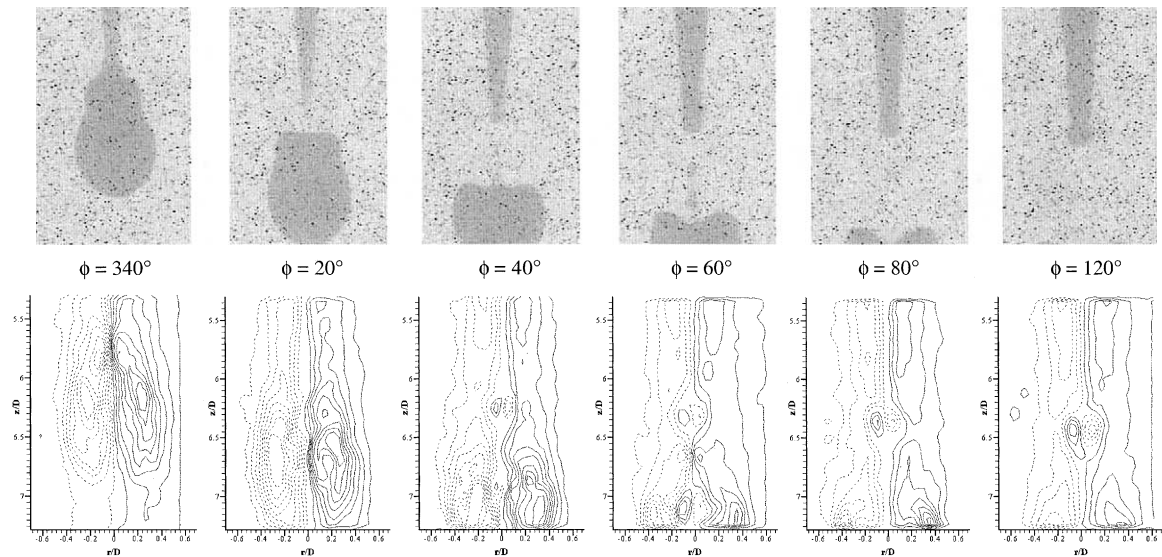

Fig. 10. Images and vorticity fields for $\lambda = 1.7$, $Re = 35$. Length of each image is 2.0D. Normalized contour levels have magnitude of 8, 16, 24, 32, 40, 48, 56, 64.

derived from individual vector plots. In this case, the outer fluid viscosity is less than the inner, and the vorticity contours are spread through both fluids. As the flow passes through the pinch off, no remarkable changes in the vorticity field are observable. The contour levels and shapes

move downstream, but remain similar from $\phi = 340°$ to $\phi = 20°$. The vorticity and its associated velocity pattern are acting to change the shape of the drop, compressing it axially. In addition, because the vorticity is centered on the interface near the pinch-off location (as opposed to being focused inside of the interface), the interface rotates at the upstream end of the developing drop (refer to the images at $\phi = 340°$ and $20°$). The interface rotation is significant at this location because the interface is already inclined with the jet axis, and the vorticity results mainly from the radial gradient in axial velocity ($\partial u/\partial r$). This is the reason for the difference in downstream interface 'angles' observed for the two flow cases at the time of pinch off. When $\lambda = 0.17$, the vorticity near the interface is relatively weak, and the interface on the upstream end of the forming drop does not rotate.

Starting at $\phi = 40°$, a small zone of 'reverse' vorticity associated with the recoiling jet tip appears. Also at this phase, the upstream end of the drop is inverted, and additional reverse vorticity is developing. By $\phi = 60°$, this zone has grown significantly. The image at $\phi = 40°$ is complicated by the presence of a satellite just upstream of the larger 'phase-locked' drop. The satellite is strained into a dumbbell shape and therefore appears to be in the process of axial contraction. The presence of the satellite most likely enhances the downstream zone of reverse vorticity. It also causes a small enhancement in 'conventional' vorticity near its upstream end. By $\phi = 80°$, the drop has nearly disappeared from the field of view, but the reverse vorticity at the jet tip persists through $\phi = 120°$.

Finally, we compare the shapes of radial velocity profiles found in the two cases examined. Radial profiles corresponding to the upstream edge of the images ($z/D = 6.15$) in Fig. 9 are plotted in Fig. 11 for five forcing phases. Note that each of the profiles exhibits a relatively sudden change in slope at a specific radial position. For example, the plots corresponding with $\phi = 240°$,
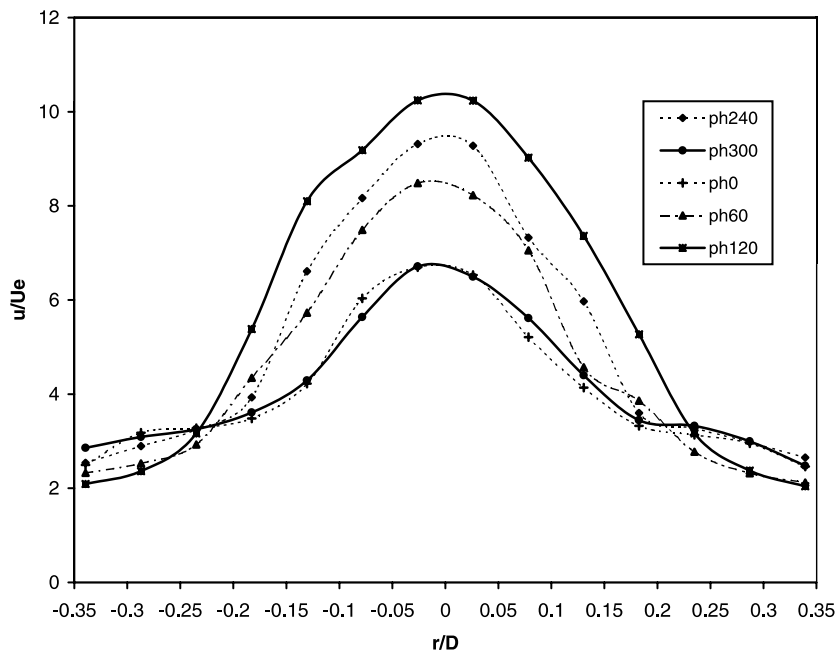

Fig. 11. Radial profiles of axial velocity for $\lambda = 0.17$, $Re = 34$, $z/D = 6.15$.

300°, and 0° all flatten at $r/D = 0.18$, while the plots of $\phi = 60°$ and 120° flatten near $r/D = 0.22$ and 0.25, respectively. The radial location of the interface for the first three phases lies near $0.11D$ (refer to the images in Fig. 9). For $\phi = 60°$ and 120°, the interface lies at $r/D = 0.18$ and 0.2, respectively. Thus, the slope discontinuity measured by PIV lies about $0.05D$ outside of the interface location in every case. We postulate that higher resolution measurements would locate the discontinuity closer to the interface location where it can be expected to occur. Specifically, one can expect that the shear stress must be continuous across the interface. Therefore, the jump in viscosity across the interface (as radius increases) must be accompanied by a sudden decrease in the local velocity gradient $\partial u/\partial r$. The slope discontinuity in the plots occurs at velocities of 2–$3U_e$. Because the velocity drops off very gradually outside of this radius, the profiles must extend far into the ambient fluid. This is, in fact, observed in profiles extracted from the lower resolution measurements associated with Figs. 4, 5 and 7 (see below).

Fig. 12 shows radial profiles for the $\lambda = 1.7$ case measured at the axial position $z/D = 6.0$. These were extracted from the 'higher resolution' PIV data associated with Fig. 10. The z/D location is close to that of pinch off. In contrast with the $\lambda = 0.17$ case, no sudden changes in slope are apparent in these profiles. Instead, they drop off smoothly such that axial velocities fall below $u/U_e = 1$ when $r/D > 0.55$. Two 'low resolution' profiles from $\lambda = 0.17$ (at a similar axial position) are included in this figure for comparison. As was shown previously, the centerline velocity is lower in general for this case. Notice, however, that the $\lambda = 0.17$ curves, because of their flatter slopes in the ambient fluid, stay above $u/U_e = 1$ until
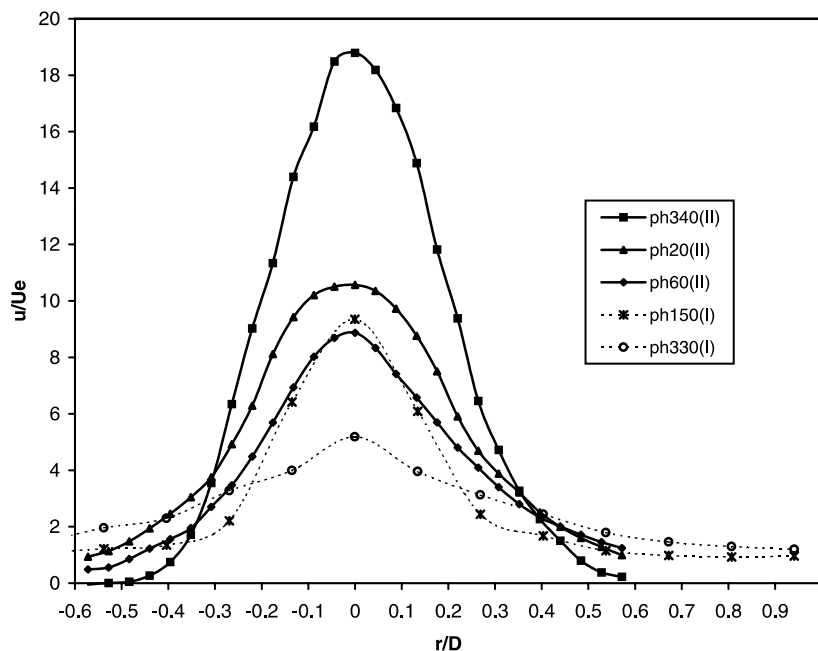

Fig. 12. Radial profiles of axial velocity for $\lambda = 1.7$, $Re = 35$, $z/D = 6.0$ (labeled as II), and for $\lambda = 0.17$, $Re = 34$, $z/D = 6.48$ (labeled as I).

$r/D \approx 0.9$. Thus, the higher viscosity ambient results in a composite jet with a broader momentum distribution.

4. Conclusions

In this paper, we have presented experimental results of flow through pinch off in round jets. The results provide documentation of the evolving velocity and vorticity fields on both sides of the fluid interface for two specific cases where viscosity ratio, gravity, inertia, surface tension, and periodic variations all play significant roles. An index matching technique was applied to two combinations of fluids in order to obtain clear instantaneous images and full two-dimensional velocity fields by PIV. The index-matching method and laser sheet illumination allowed the observation of concave curvature within droplets. The PIV method allowed velocity variations to be resolved to a scale of 1 mm on both sides of the fluid interface.

The results demonstrated that the viscosity ratio had a significant effect on the evolving jet flow, the pinch-off process, and the resulting drop shapes. Interface shapes near pinch off agreed well with the boundary integral results of Zhang and Lister (1999) that demonstrated self-similar behavior for pinching fluid threads. A lower viscosity ambient fluid yielded a jet with greater gravitational acceleration before pinch off. The jet fluid reached significantly higher velocities, and the jet diameter was smaller than in the case with higher ambient viscosity. In the pinch-off zone, the lower viscosity ambient yielded a narrower cone shape upstream and a flatter droplet shape downstream. The narrower cone shape resulted from the stronger acceleration, longer local wavelength, and greater distance between the pinch-off location and first upstream maximum in diameter in the case with lower ambient viscosity. The flatter upstream drop shape resulted directly from the broader radial vorticity distribution in the $\lambda = 1.7$ case. The vorticity distribution extended well into the ambient fluid and thus caused the upstream end of the drop to flatten by rotating before pinch off. The rotation continued after pinch off to generate droplets initially shaped like cups. In the $\lambda = 0.17$ case, the higher viscosity ambient yielded very weak velocity gradients outside of the jet, and consequently suppressed interface rotation.

After pinch off, the droplet in the lower viscosity ambient experienced much stronger oscillations than its counterpart in the higher viscosity ambient. In addition to the inverted curvature observed on the upstream side, a cusp structure developed at the location of largest diameter and propagated downstream during an oscillation. In the higher viscosity ambient, droplets maintained spheroidal shapes while exhibiting much weaker oscillations in the axial direction.

In both flow cases, recoiling of the jet tip caused local reversals in vorticity. In the case with lower ambient viscosity, reversed vorticity also occurred when the highly deformed droplet rebounded toward a more spherical shape. When present, satellite drops caused additional perturbations in the velocity and vorticity fields.

Radial velocity profiles exhibited different characteristics for the two fluid pairings. The higher viscosity ambient yielded profiles with steeper slopes in the inner fluid and shallow slopes in the ambient, a result expected from the boundary condition at the interface where the local shear stress must be continuous. Large velocities were confined to a relatively narrow radius, while small velocities extended far into the ambient. Conversely, the lower viscosity ambient yielded profiles

with more continuous slopes, but broader distributions of large velocities and significant gradients. Beyond radii of 0.2*D*, these profiles exhibited steeper gradients.

In future studies, we plan to examine the importance of the forcing frequency, forcing amplitude, and Reynolds number in determining the pinch-off behavior. Also, we plan to apply a 'super-resolution' PIV technique in order to capture velocity variations over smaller length scales. Some questions still to be answered include: what are the stability limits for various forcing cases, how do the Reynolds number and forcing amplitude affect pinch-off conditions, and what are the details of behavior associated with satellite formation?

Acknowledgements

References

Brenner, M.P., Eggers, J., Joseph, K., Nagel, S.R., Shi, X.D., 1997. Breakdown of scaling in droplet fission at high Reynolds number. Phys. Fluids 9, 1573–1590.

Bright, A., 1985. Minimum drop volume in liquid jet breakup. Chem. Eng. Res. Des. 63, 59–66.

Cohen, I., Brenner, M.P., Eggers, J., Nagel, S.R., 1999. Two fluid drop snap-off problem: experiments and theory. Phys. Rev. Lett. 83, 1147–1150.

Freeman, R.W., Tavlarides, L.L., 1979. Observations of the instabilities of a round jet and the effect of cocurrent flow. Phys. Fluids 22, 782.

Kitamura, Y., Mishima, H., Takahashi, T., 1982. Stability of jets in liquid–liquid systems. Can. J. Chem. Eng. 60, 723–731.

Longmire, E.K., Lowengrub, J.S., Gefroh, D.L., 1999. A comparison of experiments and simulations on pinch-off in round jets. In: Proceedings of the 3rd ASME/JSME Joint Fluids Engineering Conference, San Francisco, ASME FEDSM99-7111.

McKinley, G.H., Tripathi, A., 2000. How to extract the Newtonian viscosity from capillary breakup measurements in a filament rheometer. J. Rheol. 44, 653–670.

Meister, B.J., Scheele, G.F., 1967. Generalized solution of the Tomotika stability analysis for a cylindrical jet. AIChE J. 13, 682–688.

Meister, B.J., Scheele, G.F., 1969a. Prediction of jet length in immiscible liquid systems. AIChE J. 15, 689–699.

Meister, B.J., Scheele, G.F., 1969b. Drop formation from cylindrical jets in immiscible liquid systems. AIChE J. 15, 700–706.

Richards, J.R., Scheele, G.F., 1985. Measurement of laminar jet velocity distributions in liquid–liquid systems using flash photolysis. Chem. Eng. Commun. 36, 73–92.

Skelland, A.H.P., Johnson, K.R., 1974. Jet break-up in liquid–liquid systems. Can. J. Chem. Eng. 52, 732–738.

Skelland, A.H.P., Walker, P.G., 1989. The effects of surface active agents on jet breakup in liquid–liquid systems. Can. J. Chem. Eng. 67, 762–770.

Tadrist, L., Alaoui, E.K.O., Occelli, R., Pantaloni, J., 1991. Experimental study of a liquid jet flowing into another immiscible liquid 'A local analysis of the interface'. Exp. Fluids 12, 67–75.

Webster, D.R., Longmire, E.K., 2001. Jet pinch-off and drop formation in immiscible liquid/liquid systems. Exp. Fluids 30, 47–56.

Zhang, W.W., Lister, J.R., 1999. Similarity solutions for capillary pinch-off in fluids of differing viscosity. Phys. Rev. Lett. 83, 1151–1154.
Zhang, X., Basaran, O.A., 1995. An experimental study of dynamics of drop formation. Phys. Fluids 7, 1184–1202.